L. Spitzer "Physical Processes in the Interstellar medium"

computed [36] for intermediate situations where both radiation damping and Doppler broadening must be considered, giving a "Voigt profile" instead of the simpler Maxwellian.

We turn now to the observations of narrow interstellar absorption lines. The extensive ground-based data on interstellar Na I and Ca II absorption provide information on the velocity distribution of the interstellar gas [35]. Many separate components are seen in these lines, with radial velocities for some Ca II components as high as 100 km s^{-1}. The strongest components, with velocities up to about 10 km s^{-1} in the local standard of rest, generally correlate reasonably well with 21-cm emission components, but for the clouds of higher velocity the correlation is poor, with often no 21-cm emission observable at the velocity of a Ca II cloud. If a correction is made for blending, the number k of components per kpc has been estimated as between 8 and 10 [37], and with more recent higher resolution [38, 39] the number of components has been somewhat increased. Most of these components have presumably much less material in the line of sight than the absorbing H I clouds with $\tau_0 \geq 0.2$, for which a value of 4 per kpc was obtained above for k. If the clouds with weak Na I absorption are excluded, the dispersion σ_v of radial velocities between different clouds is about the same 6 km s^{-1} [29] obtained from the 21-cm data.

The effective thickness $2H$ of the gaseous galactic disk has been obtained [40] from the measured W_λ of the K line of Ca II at 3933.7Å. Since this line is relatively unsaturated, W_λ is nearly proportional to N(Ca II). Dividing N(Ca II) for a line of sight through the Galaxy, pole to pole, by the mean n(Ca II) in the galactic plane gives $2H = 240$ pc, in good agreement with the value obtained from 21-cm emission [S3.3b]. Some clouds producing measurable Ca II absorption are at much greater distances from the galactic plane; on the average, a line perpendicular to this plane intersects from 0.25 to 0.5 such clouds beyond 750 kpc and with a radial velocity exceeding 24 km s^{-1} [41].

The composition of several H I clouds has been determined [34] from measures of W_λ for many lines, mostly in the ultraviolet. The most detailed results are for the line of sight to ζ Oph ($E_{B-V} = 0.32$). A few of the interstellar lines in this star, including some lines of the dominant singly ionized atoms of Mg, P, Ni, and Fe, are on the linear part of the curve of growth, giving column densities directly from the adopted f_{ik}. For other lines a curve of growth must be used. Since there is no reason to expect that $\phi_a(\Delta\nu)$ is Maxwellian, the theoretical curve of growth discussed above is not necessarily realistic. It is necessary to construct empirical curves of growth, combining in one group those atoms which might be expected to show the same mean velocity distribution function. For example, atoms of the dominant ionization species in H I regions, such as N I, O I, Mg II,

and Si II, would be expected to have the same $\phi_a(\Delta\nu)$, provided that their relative abundances were the same in all clouds. However, neutral atoms such as Mg I and Si I, whose relative abundances should be proportional to the density, will have different abundances relative to their corresponding ions in different clouds and consequently a different $\phi_a(\Delta\nu)$ from that of Mg II and Si II. Within each group the values of $\log(W_\lambda/\lambda)$ from a variety of lines absorbed by a particular atom can be plotted against $\log(f\lambda)$ to give a section of the curve of growth. Different sections are then shifted horizontally to agree with corresponding sections found from other atoms in the same group; N_j is then determined from lines on the linear section. Figure 3.2 shows the empirical curves of growth obtained in this way for ζ Oph, indicating the difference between different groups of elements; for the triangles, representing Mg I, Si I, and neutral atoms of similar elements, the curve of growth clearly does not correspond to the theoretical curves for a Maxwellian $\phi_a(\Delta\nu)$, but it may be reproduced by several clouds with different radial velocities and widely different column densities.

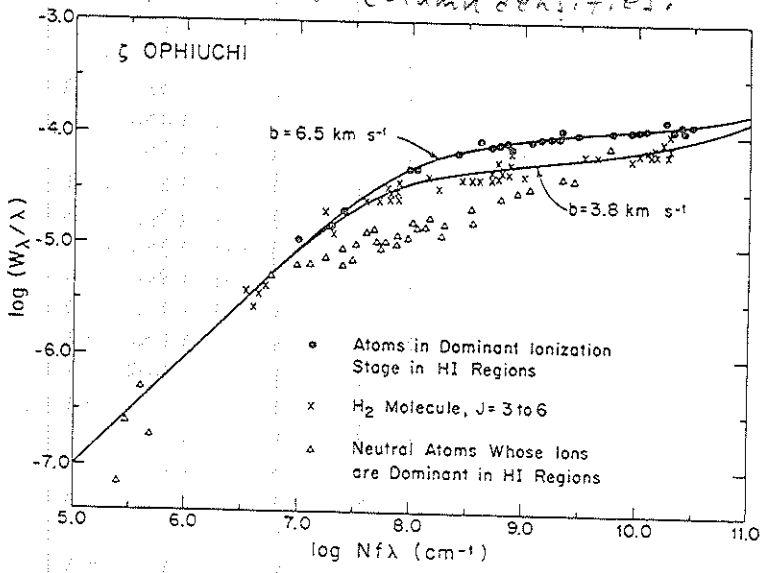

Figure 3.2 Curves of growth for interstellar lines in ζ Oph [34]. The filled circles represent lines produced by Al I, Ar I, Mg II, Si II, S II, and Fe II, representing for each element the dominant stage of ionization in an H I region. The triangles represent C I, Na I, Mg I, S I, K I, and Fe I; these are neutral atoms of elements which are mainly singly ionized in H I regions. The crosses represent H_2 Lyman lines from the levels with rotational quantum number J between 3 and 6. The two solid lines represent theoretical curves for a Maxwellian velocity distribution with the indicated values of b, equal to $2^{1/2}$ times the dispersion of radial velocities.

Regardless of whether the grains were born in stellar atmospheres or in dense interstellar clouds, the depletion found for different elements seems consistent with a relatively simple model of grain formation in a gas of decreasing temperature and density [16]. On this model, the elements with the highest condensation temperature T_c should condense first, with other elements condensing later. If the density decrease is sufficiently rapid, the fraction of atoms of each element condensing into grains will be less for the low-T_c elements than for those of high T_c. Figure 9.1 shows a plot of the depletion observed [17] in the interstellar cloud in the line of sight to ζ Oph [S3.4c]; the values of the depletion given in Table 1.1 are plotted against computed values of T_c [16]. In the computations, the gas with a temperature T is assumed to have cosmic composition and to be at a pressure of about 1000 dyne cm^{-2}. The abundances of the different molecular species are determined by the appropriate relations for thermodynamic equilibrium. The value of T at which half the atoms of a given element have condensed out in one form or another is defined as T_c. At different pressures, the values of T_c are different, but the general appearance of the plot in Fig. 9.1 is not much changed. There seems no question but that the depletions tend to be large for the elements of highest T_c.

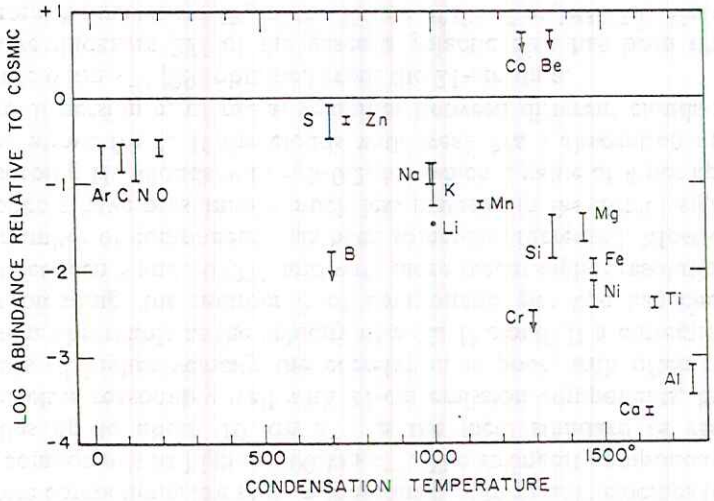

Figure 9.1 Dependence of depletion on condensation temperature [17]. The observed values of the depletion for each element observed in ζ Oph (Table 1.1) are plotted against values of the condensation temperature T_c (°K) [16], defined as the temperature at which half the atoms of an element have condensed out in one form or another in thermodynamic equilibrium. Each vertical bar represents an estimated possible error in the depletion resulting from uncertainties in the various curves of growth assumed.

One might expect that small grains composed of the more refractory materials (characterized by higher melting temperatures) might form first from condensation in a relatively dense cloud, and that mantles of CH_4, NH_3, and H_2O would form at a later time, perhaps within the denser observed diffuse clouds. The depletion of C, N, and O shown in Fig. 9.1 is somewhat uncertain, but is consistent with the apparent observed increase in grain radius with E_{B-V} in extended cloud complexes [S8.2b]. Also consistent with this point of view is the relatively slight depletion observed for N and O in more transparent clouds [S3.4c].

While the theory of initial grain condensation in a dense warm gas yields some impressive agreement with the observations, the model raises certain difficulties. The very large depletion of elements such as Ca and Ti seems easily understood if all the atoms of these elements have passed through this condensation phase. However, it is generally assumed that the atoms of these heavy elements were formed in supernovae rather than in late-type giants; it seems unlikely that almost all the heavy elements in interstellar space have passed either through stars or through dense high-temperature interstellar clouds at least once since being ejected from supernovae. In addition, the agreement shown in Fig. 9.1 is about as good if the depletion is plotted against first ionization potential, provided that the three alkali metals, Li, Na, and K, are arbitrarily excluded [18].

If one assumes that the condensation nuclei have formed somehow, the rate at which the grains grow by accretion in observed diffuse clouds can be computed on the basis of a relatively simple model. For grains with more than a certain number of atoms, one might expect that the sticking probability ξ_a for most atoms would be not far below unity. Physical adsorption to the surface, which requires no activation energy, should be possible, and an atom colliding with the grain is likely to give up enough of its kinetic energy so that it will become bound. Detailed analysis [19] confirms that $\xi_a \approx 1$ for neutral atoms, although important uncertainties remain for C^+ and other positive ions.

We compute now the rate at which the grain radius a will grow by this accretion process. If m_d denotes the mass of the grain, while the particle density, mass, and velocity of the colliding atoms are denoted by n_a, Am_H, and w_a, respectively, and if the loss processes considered below are ignored, the rate of mass accretion by the grains becomes

$$\frac{dm}{dt} = \pi a^2 w_a n_a A m_H \xi_a, \tag{9-28}$$

THE ASTROPHYSICAL JOURNAL, 585:638–646, 2003 March 10

HEAVY-ELEMENT ABUNDANCES AND DUST DEPLETIONS IN THE HOST GALAXIES OF THREE GAMMA-RAY BURSTS

SANDRA SAVAGLIO[1]
Johns Hopkins University, 3400 North Charles Street, Baltimore, MD 21218; savaglio@pha.jhu.edu

S. MICHAEL FALL
Space Telescope Science Institute, 3700 San Martin Drive, Baltimore, MD 21218; fall@stsci.edu

AND

FABRIZIO FIORE
Osservatorio Astronomico di Roma, via di Frascati 33, Monteporzio I-00040, Italy; fiore@quasar.mporzio.astro.it
Received 2002 March 11; accepted 2002 November 20

ABSTRACT

We have derived the column densities of heavy elements in three gamma-ray burst (GRB) optical transients, associated with the circumburst or interstellar medium (ISM) of the host galaxy. In comparison with the same elements observed in damped Lyα (DLA) systems along QSO sight lines, we find evidence for much higher column densities of Zn II. The gap between the QSO-DLA and GRB-DLA distributions is smoothly bridged by observations of the interstellar absorption in the Milky Way and the Magellanic Clouds. Very small [Fe/Zn], [Si/Zn], and [Cr/Zn] values in GRB-DLAs indicate large dust depletions. Once the dust-to-metals ratios are determined, we find an optical extinction $A_V \approx 1$ mag, to be compared with typical $A_V \lesssim 0.1$ in most QSO-DLAs. Our inference of high dust content appears to be in contradiction with the typical low reddening previously found in GRBs. One possible way to reconcile is a dust grain size distribution biased toward big grains, which would give a gray extinction. Possibly, the small dust grains have been destroyed by the GRBs themselves. Our findings support the idea that primarily optically selected QSOs probe mainly low-gas/dust regions of high-redshift galaxies, while the more powerful GRBs can be detected through denser regions of their ISM (molecular clouds and star-forming regions). Therefore, GRB-DLAs and QSO-DLAs together provide a more complete picture of the global properties of the interstellar medium in high-redshift galaxies.

Subject headings: cosmology: observations — dust, extinction — gamma rays: bursts — intergalactic medium — quasars: absorption lines

On-line material: color figures

1. INTRODUCTION

Gamma-ray bursts (GRBs) are among the most dramatic events in the universe. Their luminosities are so high (10^{51}–10^{54} ergs are emitted in a few seconds) that they can be seen at the highest redshifts. However, since the decline in their energy emission is very fast, the investigation and understanding of their physical nature is not particularly easy (Piran 2003). For instance, the redshift of the afterglow or host galaxy has been measured in only 24 cases.[2]

Only eight of these objects have been targeted quickly enough by ground-based telescopes to obtain low-resolution spectra of the optical transient, and all show a common peculiarity: very strong UV absorption lines of low-ionization species (Fiore 2001; Fynbo et al. 2002). This is similar to what is seen in damped Lyα systems (DLAs) associated with intervening galaxies along QSO sight lines. GRB-DLAs are certainly an unexplored and important source of information on the circumburst and/or interstellar medium (ISM) of the GRB host galaxy. Here we explore in more detail their properties and compare them with those of QSO-DLA galaxies.

We use the curve-of-growth (COG) analysis to derive column densities of low-ionization species in several GRB-DLAs. As for QSO-DLAs, we neglect ionization effects to derive the abundances of several heavy elements. The low ionization of the gas is warranted by the large equivalent widths of the low-ionization lines and the low equivalent widths of the moderate- and high-ionization lines. The difference in abundances between weakly and greatly dust-depleted elements provides an estimate of the dust content.

The COG analysis was applied to QSO-DLAs (Blades et al. 1982; Turnshek et al. 1989) before the advent of high-resolution spectroscopy, which allows a direct fitting of individual absorption lines. Since GRB emission fades very rapidly, high-resolution (FWHM ~ 10 km s^{-1}) spectra of GRB afterglows are very hard to obtain.

In this work, we interpret strong differences between GRB-DLAs and QSO-DLAs as the result of the difference in the densities of the intervening gas. Since GRBs are, at least for some time, brighter than primarily optically selected QSOs, they can be observed even if their sight lines cross very dense and dusty regions, such as molecular clouds, where extinction is very severe. On the other hand, QSO sight lines are easier to detect when intersecting less dusty interstellar clouds.

This bias in QSO-DLAs has been already suggested in the past (see, e.g., Fall & Pei 1993; Boissé et al. 1998). More recently, Ellison et al. (2001) have studied a small sample of

[1] On leave of absence from Osservatorio Astronomico di Roma, Italy.
[2] See http://www.mpe.mpg.de/~jcg/grbgen.html for the complete list of GRB redshifts.

radio-selected QSOs and tentatively found more DLAs than in optically selected QSOs. Even if this result is affected by small number statistics (significant at $\sim 2\,\sigma$ level), it supports the idea of dust obscuration in optically selected QSO-DLAs.

Our analysis is alternative to and independent of the dust content estimate obtained so far for GRBs. The dust reddening in GRB afterglows has been derived in several objects (see, e.g., Reichart 1998; Jensen et al. 2001; Rhoads & Fruchter 2001; Fynbo et al. 2001; Galama & Wijers 2001), and in most cases it has been found to be small or negligible. The method applied assumes initial power-law emission from the GRBs and steep extinction curves such as those in the Milky Way (MW) or Large and Small Magellanic Clouds (MCs). Possible discrepancies with the results of our analysis challenge the two initial assumptions of very steep extinction and initial power-law emission of the central source.

For this study, we examine the absorption lines of three of the eight GRBs with UV rest-frame spectra, namely, GRB 990123 ($z = 1.601$; Kulkarni et al. 1999), GRB 010222 ($z = 1.475$; Masetti et al. 2001; Jha et al. 2001; Salamanca et al. 2001; Mirabal et al. 2002), and GRB 000926 ($z = 2.0379$; Castro et al. 2003). We exclude GRB 970508 ($z = 0.835$; Metzger et al. 1997), GRB 990510 ($z = 1.619$; Vreeswijk et al. 2001), GRB 000301C ($z = 2.04$; Jensen et al. 2001), GRB 990712 ($z = 0.4331$; Vreeswijk et al. 2001), and GRB 011211 (Holland et al. 2002) for poor quality of the spectra and therefore lack of interesting absorption features.

2. GRB-DLA COLUMN DENSITY DETERMINATION

Similarly to QSO-DLAs, GRB-DLAs show strong Fe II, Mg II, and Si II absorptions, together with relatively weak Zn II and Cr II. Table 1 lists oscillator strengths f_λ (from the recent compilation by Prochaska et al. 2001) and rest-frame equivalent widths W_r of absorption lines in the three GRBs used in the present analysis. The large W_r of all these species relative to higher ionization species such as C IV, Si III, and Si IV indicate that the medium is weakly ionized. From the equivalent widths (EWs), we derive column densities and directly compare the results with typical column densities in QSO-DLAs. Comparing column densities instead of metallicities [X/H] has the advantage that the H I column density (known only in GRB 000926 with large uncertainty; Fynbo et al. 2002) is not required. Moreover, it is not necessary to make any assumptions about the dust depletion, cosmic abundance, or ionization level of the considered element, but we can still search for similarities and differences between GRB-DLAs and QSO-DLAs.

A direct comparison is complicated by the fact that normally QSO-DLAs are observed at high spectral resolution (FWHM $\simeq 10$ km s^{-1}) in a large wavelength range (thanks to echelle spectroscopy), allowing a good determination of

TABLE 1

REST-FRAME EQUIVALENT WIDTHS

		W_r (Å)		
LINE	f_λ	GRB 990123 ($z = 1.6004$)	GRB 000926 ($z = 2.038$)	GRB 010222 ($z = 1.475$)
Zn II λ2026	0.489	0.800 ± 0.065	0.900 ± 0.067	$0.79^{+0.05}_{-0.07}$ [a,b]
Zn II λ2062	0.256	0.485 ± 0.038[c]	<0.28[d]	0.41 ± 0.05[a,e]
Si II λ1526	0.127	...	2.64 ± 0.18	1.53 ± 0.09[f]
Si II λ1808	0.00218	...	1.130 ± 0.089	0.55 ± 0.02[f]
Cr II λ2056	0.105	...	0.690 ± 0.050	0.35 ± 0.03[g]
Cr II λ2066	0.0515	...	<0.2	0.31 ± 0.08[g]
Cr II λ2062	0.078	...	<0.28[d]	0.32 ± 0.04[a,e]
Fe II λ1608	0.058	...	2.15 ± 0.16	0.47 ± 0.04[g]
Fe II λ2260	0.00244	...	...	0.52 ± 0.18[h]
Fe II λ2344	0.114	1.17 ± 0.11	3.41 ± 0.24	1.92 ± 0.04[i]
Fe II λ2374	0.0313	...	2.57 ± 0.20	1.60 ± 0.06[j]
Fe II λ2382	0.320	1.38 ± 0.15	3.07 ± 0.31	2.35 ± 0.06[j]
Fe II λ2586	0.0691	1.09 ± 0.14	...	1.53 ± 0.05[f]
Fe II λ2600	0.239	1.338 ± 0.054	3.65 ± 0.26	2.31 ± 0.06[f]
Mn II λ2576	0.3508	...	...	0.60 ± 0.05[f]
Mn II λ2594	0.2710	...	...	0.68 ± 0.09[a]
Mn II λ2606	0.1927	...	...	0.56 ± 0.12[h]

[a] Weighted mean from Jha et al. 2001, Salamanca et al. 2001, and Mirabal et al. 2002.
[b] Lower error found assuming possible contamination from Mg I λ2026 line.
[c] Cr II λ2062 contribution to the Zn II λ2062 + Cr II λ2062 blend is negligible.
[d] Noisy region of the spectrum, given only upper limit based on the total EW + 3 σ, reported by Castro et al. 2003.
[e] Contribution of the Cr II λ2062 line to the Zn II λ2062 + Cr II λ2062 blend calculated using the Cr II column density as derived from Cr II λλ2056, 2066.
[f] Weighted mean from Masetti et al. 2001, Salamanca et al. 2001, Jha et al. 2001, and Mirabal et al. 2002.
[g] Weighted mean from Salamanca et al. 2001 and Mirabal et al. 2002.
[h] Mirabal et al. 2002.
[i] Weighted mean from Masetti et al. 2001, Jha et al. 2001, and Mirabal et al. 2002.
[j] Weighted mean from Jha et al. 2001 and Mirabal et al. 2002.

column densities of many ions, even in cases where saturated or weak lines in complex features are detected (see, e.g., Lu et al. 1996; Pettini et al. 1997; Prochaska & Wolfe 1999). On the other hand, the typical resolution of GRB optical spectra is FWHM > 100 km s^{-1}. Moreover, the majority of absorption lines are saturated, and it is not possible to use the linear part of the COG to determine column densities. However, the lines are numerous, so even if the uncertainty may be large, it is possible to make an abundance analysis using the general COG analysis (Spitzer 1978). Since the typical resolution of GRB spectra does not allow the separation of the different components of a complex feature, because of the many clouds along the line of sight, in our analysis we adopt a large "effective" Doppler parameter, being the result of the superposition of many narrow absorption lines. For reference, we note that typical velocities in QSO-DLAs are ~100 km s^{-1} or more. The COG analysis applied with the single-component approximation was used for QSO-DLA studies before high-resolution spectroscopy of QSOs became possible (see, e.g., Blades et al. 1982; Turnshek et al. 1989). In fact, Jenkins (1986) showed that the COG technique applied to complex features gives nearly the correct answer (the simulated-to-true column density ratio rarely goes below 0.8) even if different lines have very different saturation levels or Doppler parameters. This general result is also confirmed by Savage & Sembach (1991).

The best-fitting column density is determined by using simultaneously different EWs of various ions and choosing the COG with an effective Doppler parameter that minimizes the χ^2. Once the best effective Doppler parameter is determined, the error on the column density for each ion is determined by varying $\log N$ for which $\chi^2/\mathrm{dof} \lesssim 1$. In the following §§ 2.1–2.3, we discuss column density measurements in each individual GRB. Figures 1, 2, and 3 show the best-fitting W_r/λ and column densities and the corresponding COG. Estimated column densities are given in Table 2.

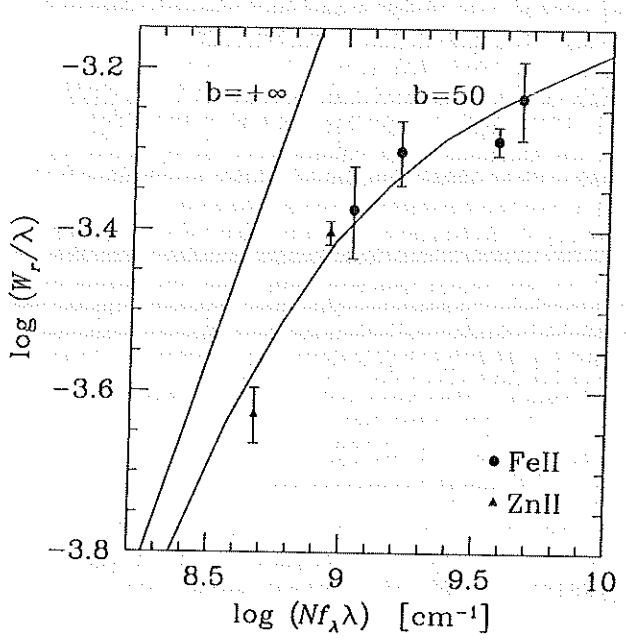

FIG. 1.—COG for GRB 990123 absorption lines (b is the effective Doppler parameter in km s^{-1}). Points give the best-fit column densities, reported in Table 2. The straight line is the linear case ($b = +\infty$). [*See the electronic edition of the Journal for a color version of this figure.*]

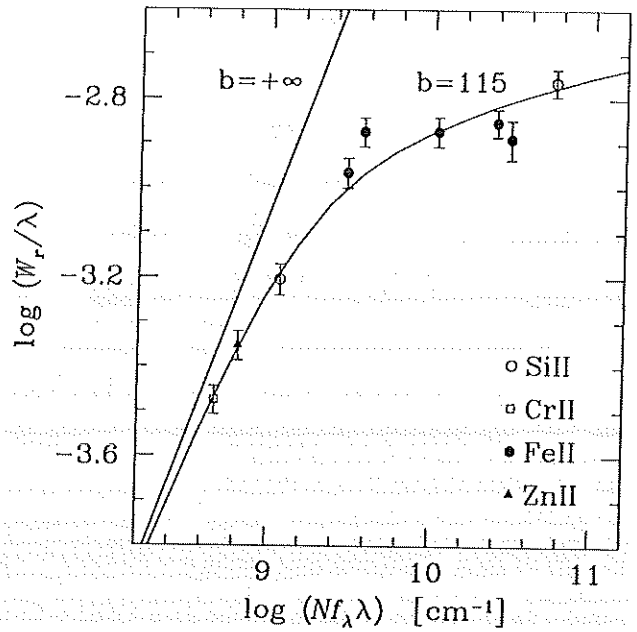

FIG. 2.—Same as Fig. 1 but for GRB 000926 absorption lines. [*See the electronic edition of the Journal for a color version of this figure.*]

2.1. *GRB 990123*

The optical transient of GRB 990123 at $z = 1.6004$ was observed with the Keck/Low Resolution Imaging Spectrograph (LRIS; Kulkarni et al. 1999) for a final resolution and signal-to-noise ratio (S/N) of FWHM = 11.6 Å (400–700 km s^{-1}) and S/N ≈ 30, respectively. The very weak Fe II

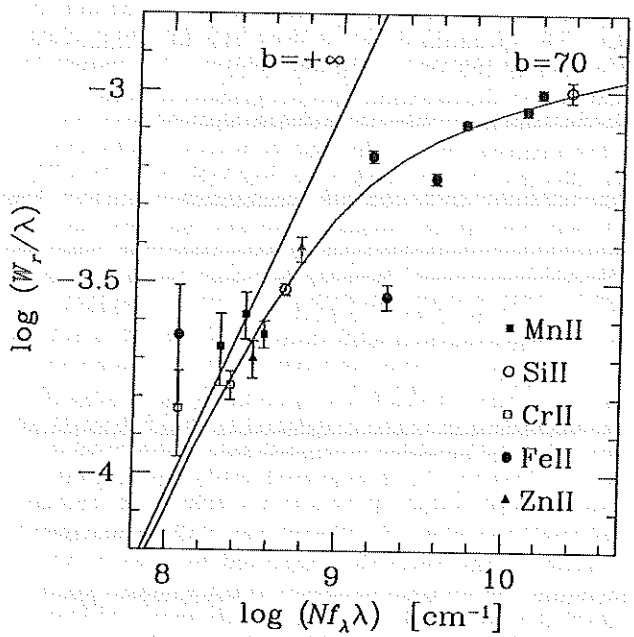

FIG. 3.—Same as Fig. 1 but for GRB 010222 absorption lines. [*See the electronic edition of the Journal for a color version of this figure.*]

TABLE 2
COLUMN DENSITIES

Ion	log N(X) (cm^{-2}) GRB 990123	GRB 000926	GRB 010222
Zn II	$13.95^{+0.05}_{-0.05}$	$13.82^{+0.05}_{-0.05}$	13.78 ± 0.07
Si II.....	...	$16.47^{+0.10}_{-0.15}$	16.09 ± 0.05
Cr II.....	...	$14.34^{+0.05}_{-0.05}$	$14.04^{+0.04}_{-0.06}$
Fe II.....	$14.78^{+0.17}_{-0.10}$	$15.60^{+0.20}_{-0.15}$	$15.32^{+0.13}_{-0.10}$
Mn II...	...	...	$13.61^{+0.08}_{-0.06}$

λ2260 EW gives inconsistent results with other Fe II lines, and thus this detection has not been considered in our analysis. Fe II λ2374 is not reliable because it is probably partly blended with the Fe II λ2382 line.

For the four remaining Fe II lines, we get a best fit of $\log N(\mathrm{Fe\ II}) = 14.78^{+0.17}_{-0.10}$ and $b = 50$ km s^{-1} (Fig. 1). From the EW of Zn II λ2026 and considering $b = 50$ km s^{-1}, we derive a Zn II column density of $\log N(\mathrm{Zn\ II}) \simeq 14$ and calculate a Zn II λ2062 contribution to the Zn II λ2062 + Cr II λ2062 blend of $W_r = 0.58$ Å, to be compared with the detected $W_r = 0.48 \pm 0.04$ Å. This means that the contribution of the Cr II λ2062 line to the blend is negligible or nonexistent. Therefore, we recalculate the Zn II column density from the Zn II λ2026 and Zn II λ2062 doublet, from which we derive $\log N(\mathrm{Zn\ II}) = 13.95^{+0.05}_{-0.05}$.

2.2. *GRB 000926*

GRB 000926 at $z = 2.0379$ was observed with the Keck/Echelle Spectrograph and Images (ESI; Castro et al. 2003), with a good S/N (=10–20) and relatively high resolution (FWHM $\approx$ 80 km s^{-1}). Castro et al. (2003) also show a low-resolution spectrum, with EW measurements that are systematically larger than those obtained from the high-resolution spectrum, but the authors claim that the high-resolution measurements are more accurate, so we only use these. The spectrum shows at least two absorbing clouds separated by 168 km s^{-1}. In our analysis, we consider the total EWs of the two components together, since the resolution does not allow them to be clearly separated.

The observed Si II λ1808 and Si II λ1526 lines and the five detected Fe II lines give $\log N(\mathrm{Si\ II}) = 16.47^{+0.10}_{-0.15}$ and $\log N(\mathrm{Fe\ II}) = 15.6^{+0.20}_{-0.15}$, respectively ($b = 115$ km s^{-1}; Fig. 2). If we assume $b = 115$ km s^{-1}, we get $\log N(\mathrm{Cr\ II}) = 14.34^{+0.05}_{-0.05}$ from the Cr II λ2056 EW. This corresponds to $W_r = 0.5$–0.6 Å and $W_r = 0.35$–0.43 Å for Cr II λ2062 and Cr II λ2066, respectively. Neither of these measurements is consistent with those observed ($W_r < 0.28$ Å and $W_r < 0.2$ Å, respectively); this might indicate a contamination of the Cr II λ2056 line by an unidentified absorption associated with an intervening metal system. Moreover, the Cr II λ2062 is probably corrupted by a noise spike in the spectrum (see Fig. 3 of Castro et al. 2003) probably due to a remnant of the strong sky line at $\lambda = 6258.05$ Å. The same contamination might also effect the Zn II λ2062 line (the EW is inconsistently lower than expected from Zn II λ2026); therefore, the Zn column density is determined from Zn II λ2026 only: $\log N(\mathrm{Zn\ II}) = 13.82 \pm 0.05$ for $b = 115$ km s^{-1}. The lack of Fe II λ2586 detection is puzzling. If, for instance, we assume W_r(Fe II λ2586) < 1 Å (way above the detection limit in the spectrum), the line is almost unsaturated, and $\log N(\mathrm{Fe\ II}) < 14.6$ for $b > 70$ km s^{-1}, inconsistent with what is found from the other Fe II lines.

Fynbo et al. (2001) report a tentative H I column density measurement of $N(\mathrm{H\ I}) \approx 2 \times 10^{21}$ cm^{-2}. This leads to a relatively high metallicity with [Zn/H] $\simeq -0.13$.

2.3. *GRB 010222*

The optical transient of GRB 010222 at $z = 1.475$ was observed with the Fred Lawrence Whipple Observatory 1.5 m telescope (Jha et al. 2001; FWHM = 6 Å or 300–450 km s^{-1}, S/N $\simeq$ 10), with the 3.58 m Telescopio Nazionale Galileo (Masetti et al. 2001; FWHM = 4.8 Å or 200–400 km s^{-1}, S/N = 10–20), with the 4.2 m William Herschel Telescope (Salamanca et al. 2001; FWHM = 3.3–5.8 Å or $\sim$300 km s^{-1}, S/N $\simeq$ 10), and with Keck/LRIS and ESI (Mirabal et al. 2002; FWHM = 11–13 Å or $\sim$650 km s^{-1}, and FWHM = 0.4–0.8 Å or $\sim$30 km s^{-1}). Even though the different spectra span a time interval of $\sim$27 hr, starting 5 hr after the burst, the absorption-line EWs do not show significant time variability (Mirabal et al. 2002). Therefore, to obtain a better estimate of column densities, we combined the EWs of the same lines from different observations weighted according to the errors. We constrain the effective Doppler parameter to $b = 70$ km s^{-1}, using the Si II λ1526 and Si II λ1808 lines and seven Fe II lines (Fig. 3). We get $\log N(\mathrm{Si\ II}) = 16.09 \pm 0.05$ and $\log N(\mathrm{Fe\ II}) = 15.32^{+0.15}_{-0.10}$. The Fe II lines are scattered in the COG diagram, probably because of nonuniform EW measurements by the four groups.

The Zn II λ2026 line at $\lambda \approx 5018$ Å is blended with the Mg I λ2026 line. The contamination of Mg I to this doublet is estimated using the Mg I λ2852 line at $\lambda \approx 7065$ Å and W_r(Mg I λ2852) = 1.22 ± 0.04 Å. Assuming an effective Doppler parameter $b > 35$ km s^{-1}, we get $\log N(\mathrm{Mg\ I}) < 14$ and W_r(Mg I λ2026) < 0.04 Å. We then assume that the feature at $\lambda \approx 5018$ Å is dominated by the Zn II λ2026 absorption, with $W_r = 0.79^{+0.05}_{-0.07}$ Å and the lower error determined by a possible contamination from Mg I λ2026.

The Cr II λ2056 EW is very low; therefore, it must be weakly or not at all saturated. From the Cr II λ2056 and Cr II λ2066 lines, we get $\log N(\mathrm{Cr\ II}) = 14.04^{+0.04}_{-0.06}$. From this, we calculate a contribution of Cr II to the Zn II λ2062 + Cr II λ2062 doublet of W_r(Cr II λ2062) = 0.32 ± 0.04 Å. For this doublet we use only the measurements given by Jha et al., Salamanca et al., and Mirabal et al. (weighted mean $W_r = 0.73 \pm 0.02$ Å) because the spectrum by Masetti et al. shows strong blending with other absorption lines. Once the Cr II contribution is taken into account, we derived W_r(Zn II λ2062) = 0.41 ± 0.05 Å. Using also the Zn II λ2026 detection, we obtain $\log N(\mathrm{Zn\ II}) = 13.78 \pm 0.07$ for $b = 70$ km s^{-1}. The Mn II column density is obtained from the Mn II $\lambda\lambda$2576, 2594, 2606 triplet. For $b = 70$ km s^{-1}, we get $\log N(\mathrm{Mn\ II}) = 13.61^{+0.08}_{-0.06}$.

3. HEAVY-ELEMENT ABUNDANCES IN GRB-DLAs

Figure 4 displays the QSO-DLA column density histograms[3] of Fe II, Cr II, Zn II, and Si II. These column densities

[3] We have not used Al II measurements detected in GRB 000926 and GRB 010222 because not included in the QSO-DLA sample and because [Fe/Al] = -0.3 ± 0.3 and -0.4 ± 0.2 for GRB 000926 and GRB 010222, respectively, which is not particularly interesting for our discussion.